Real-time discrimination of earthquake foreshocks and aftershocks

ARTICLE

https://doi.org/10.1038/s41586-019-1606-4

Real-time discrimination of earthquake foreshocks and aftershocks

Laura Gulia[1]* & Stefan Wiemer[1]

Immediately after a large earthquake, the main question asked by the public and decision-makers is whether it was the mainshock or a foreshock to an even stronger event yet to come. So far, scientists can only offer empirical evidence from statistical compilations of past sequences, arguing that normally the aftershock sequence will decay gradually whereas the occurrence of a forthcoming larger event has a probability of a few per cent. Here we analyse the average size distribution of aftershocks of the recent Amatrice–Norcia and Kumamoto earthquake sequences, and we suggest that in many cases it may be possible to discriminate whether an ongoing sequence represents a decaying aftershock sequence or foreshocks to an upcoming large event. We propose a simple traffic light classification to assess in real time the level of concern about a subsequent larger event and test it against 58 sequences, achieving a classification accuracy of 95 per cent.

All crustal moderate-to-large earthquakes are followed by a decaying aftershock sequence that typically lasts for years. In some cases, this decaying sequence is interrupted by an even larger, and often more destructive, subsequent mainshock. One of the biggest unknowns in real-time seismic hazard assessment during an ongoing seismic sequence is whether the largest event—the mainshock—has already happened or is still to come. There are no scientific means yet to prospectively distinguish between 'classical' aftershock sequences and a sequence of potential foreshocks to an upcoming larger event[1,2]—the latter being typically the biggest concern of the local population and civil protection authorities. So far, the only answer that science can offer to this first-order question is a purely statistical one, based on compilations of empirical observations: the chance that after a moderate earthquake an even larger event will occur within five days and 10 km is typically 5%[3,4]. These numbers are at the core of existing systems for operational earthquake forecasting[5,6] using algorithms such as ETAS (epidemic type aftershock sequences)[7,8] or STEP (short-term earthquake probability)[9].

From the physics point of view, the probability of a subsequent larger mainshock must depend on the stress conditions set up by the previous events and the long-term tectonic stress conditions[10,11]. These conditions, as well as the location of potential faults, are typically unknown, and physics-based approaches employing Coulomb stress transfer have so far not been successful in forecasting upcoming mainshocks any better than statistical models[12], whereas their information gain is typically too low to warrant action[13,14]. There have been a number of attempts to identify foreshocks using waveform analysis or other precursory phenomena[15–17] but these have not yet resulted in improved earthquake forecasting abilities.

Here we use the fact that the time after a moderate or larger mainshock is the most data-rich period during the earthquake cycle, with thousands of aftershocks (or potential foreshocks) occurring within hours. These events allow observing spatial and temporal transients at resolutions 1,000–10,000 times higher than during normal conditions. Measuring changes in the stress caused by the mainshock is possible only indirectly and with somewhat low precision. The average size distribution of earthquakes—that is, the b value of the Gutenberg–Richter law[18,19] ($\log N = a - bM$ where N is the cumulative number of events above magnitude M, a describes the productivity and b the average size distribution of the earthquakes)—is sensitive to differential stress; its inverse dependence on differential stress has been confirmed many times in both laboratory[20–22] and field[23] studies. Recently, analysis of a stack of 58 aftershock sequences from California, Japan, Italy and Alaska—31 of them with data of good enough quality and sufficient abundance for subsequent stacking—showed that the b value of aftershock sequences generally increases after the mainshock by 20%[24]. This study also presented a Coulomb stress-based model explaining the observed transients and their dependence on magnitude, distance and faulting styles.

We propose that sequences diverting from the generally observed increased b value after a mainshock are those of high concern, for which a subsequent larger event is likely to occur. Therefore, real-time monitoring of the b value in aftershock sequences can be used for real-time discrimination between foreshocks and aftershocks, allowing us to use a posteriori awareness for a priori alerts. Evidence supporting our hypothesis comes from investigating time series of two recent sequences: the $M = 6.6$ Norcia and $M = 7.3$ Kumamoto sequences, which occurred in 2016 and were preceded by subsequently identified foreshocks reaching magnitude 6.

Establishing transients in *b* values

Computing reliable time series of the b value in aftershock zones is especially difficult, mostly because the quality, consistency and completeness of the seismicity catalogue is typically strongly affected by changes in the recording seismic network and by limitations in detection[25]. Therefore, the first hours or even days of data after a magnitude 6 event usually need to be excluded from the analysis, which is only feasible in areas with very good network coverage and advanced seismic data analysis procedures. In addition, it is often challenging to establish the local pre-mainshock b values because of the sparseness of seismicity outside sequences and limitations in recording homogeneity. The detailed analysis procedure that we follow to compute the change in b before and after the mainshock is described in Methods. We select events within 3 km of the fault plane because these have been shown to be the most reactive to stress changes[24].

The Amatrice–Norcia sequences. On 24 August 2016, an earthquake with moment magnitude $M_w = 6.2$ struck on Amatrice, central

[1]Swiss Seismological Service, ETH Zurich, Zurich, Switzerland. *e-mail: lgulia@ethz.ch

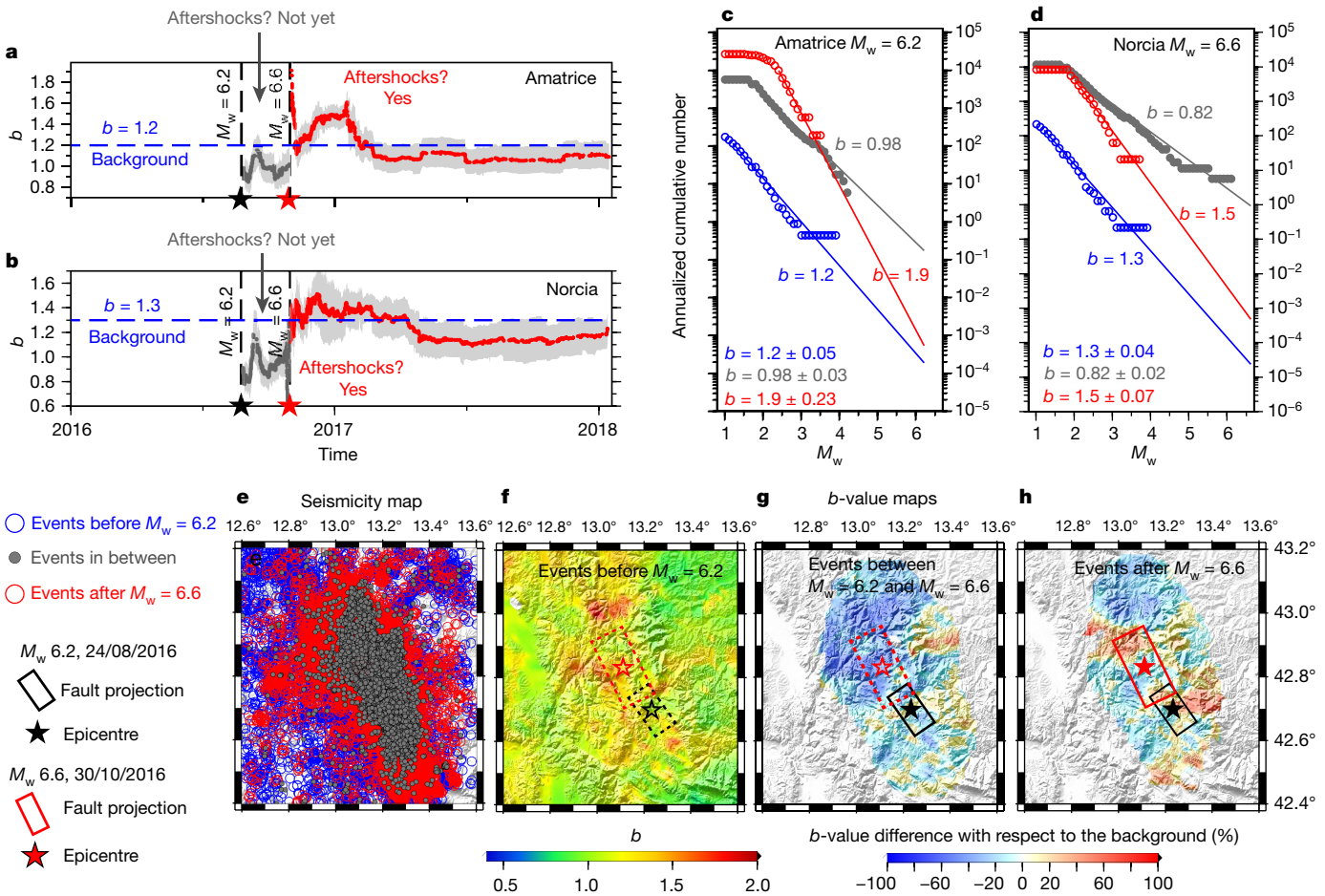

Fig. 1 | Time–space analysis of *b* values for the Amatrice–Norcia sequence. a, **b**, Time series of *b* values for the source regions of the Amatrice and Norcia mainshocks. The dashed blue lines indicate the background *b* values, and the vertical dashed grey lines represent the time of the $M_w = 6.2$ (Amatrice) and $M_w = 6.6$ (Norcia) earthquakes. The grey shaded areas show the uncertainty determined by bootstrapping (corresponding to one standard deviation). **c**, **d**, Frequency–magnitude distributions for the two source regions in three different periods (uncertainties from Shi and Bolt[47]). **e**, **f**, Seismicity maps, colour-coded by period (**e**) and pre-mainshock *b* value (**f**). **g**, **h**, Maps showing the change in the *b* value with respect to the background for the period between the two mainshocks (**g**) and the first two weeks of aftershocks (**h**).

Italy, killing about 300 people and severely damaging the town and neighbouring area. In contrast to most mainshocks in the region (for example, the 2009 $M_w = 6.3$ L'Aquila event[14]), the $M_w = 6.2$ event was not preceded by noticeable foreshocks. "Was this the mainshock?" is what the public, civil protection authorities and decision-makers were wondering at that time. It was not—two months later, on 30 October 2016, an $M_w = 6.6$ earthquake hit the town of Norcia, 20 km north-west of Amatrice, and neighbouring areas, revealing a posteriori that the $M_w = 6.2$ event and its 'aftershock' sequence were in fact foreshocks. This event was the strongest shock that occurred in the central–northern Apennines during the instrumental era[26].

Assuming near-real-time conditions, we processed events from 2012 from the Italian earthquake catalogue that is homogeneous in terms of moment magnitudes[27]. We estimated a reference *b* value for the background ($b = 1.2$ for the interval between 2012 and the last event preceding the $M_w = 6.2$ earthquake). Using an automated quality and completeness analysis (see Methods), cross-checked by visual inspection, we then removed the events in the first three days following the $M_w = 6.2$ event and computed the difference in *b* with respect to the background value (Fig. 1). After the 24 August 2016 $M_w = 6.2$ event, the *b* values near the Amatrice fault decreased by about 10%, from 1.2 to 1.1 (Fig. 1a)—a behaviour very different from the 20% increase observed generally. The plot of the frequency–size distribution of the earthquakes (Fig. 1c) shows that the decrease in *b* is stable according to high-quality data and does not depend on the chosen magnitude of completeness.

It also illustrates that the probability of a magnitude 6.6 event, inferred from the recurrence time[28], has increased by about a factor of 30. An even stronger decrease in *b* value is observed in the rupture area of the subsequent Norcia earthquakes (Fig. 1b), where the drop in *b* value is closer to 20% and the probability of a subsequent event of magnitude 6.6 increases by a factor of 1,000 over the background (Fig. 1d). To analyse the spatial footprint of the change in *b* value, we map the percentage differences from the regional *b* value. We compute *b* values on a 2-km-spaced grid, sampling the nearest 250 events to each grid node and re-estimating the completeness in each node (see Methods). The mapping results are very consistent with the series analysis and frequency–magnitude distributions. In the time between the Amatrice and Norcia mainshocks, the *b* value decreased to the north of Amatrice by 20–50% (Fig. 1g).

The picture changes markedly after the $M_w = 6.6$ Norcia event; the *b* values in the Norcia and Amatrice source areas increase by 20–30% (Fig. 1a, b). Although the Norcia aftershock sequence includes many small events (owing to its larger magnitude), the chance of a subsequent larger event is substantially smaller than in the intervening period, close to the tectonic background rate. The differential map (Fig. 1h) also reveals that the *b* values increase in most regions. Analysis of the *b* values thus suggests that after the Norcia mainshock, typical aftershock activity is taking place, in agreement with the generic model. Indeed, until now (February 2019), no secondary large mainshock or larger event has taken place, although this was a highly concerning scenario in the autumn of 2016.

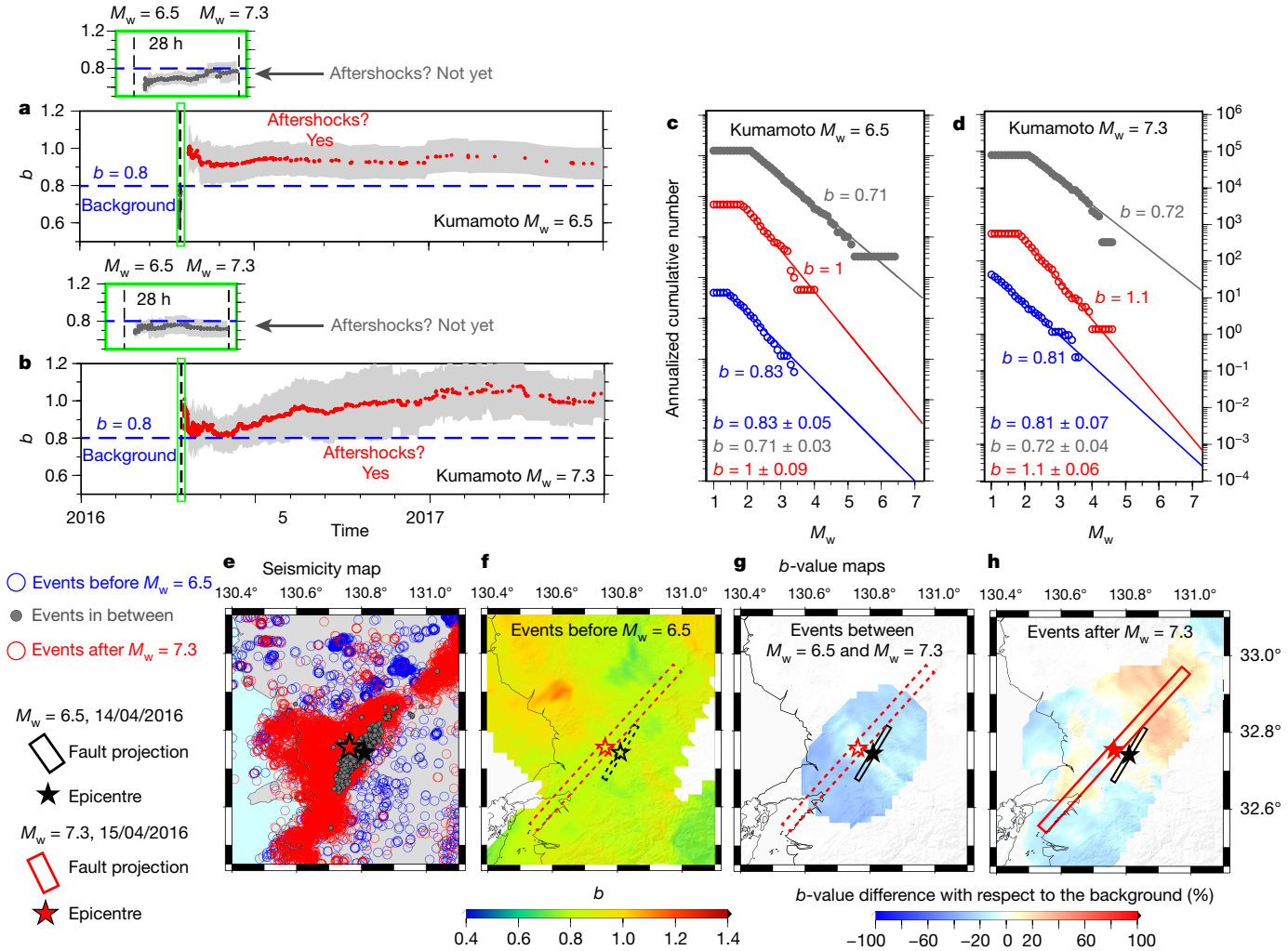

Fig. 2 | Time–space analysis of *b* values for the Kumamoto sequence. **a**, **b**, Time series of *b* values for the source regions of the $M_w = 6.5$ and $M_w = 7.3$ events. The dashed blue line shows the background *b* values and the vertical dashed grey lines represent the time of the $M_w = 6.2$ and $M_w = 7.3$ earthquakes. The grey shaded areas represent the uncertainty determined by bootstrapping. **c**, **d**, Frequency magnitude distributions for the two source regions in three different periods (uncertainty from Shi and Bolt[47]). **e**, **f**, Seismicity maps, colour-coded by period (**e**) and pre-mainshock *b* value (**f**). **g**, **h**, Map showing the change in the *b* value with respect to the background for the period between the two mainshocks (**g**) and the first two weeks of aftershocks (**h**).

The Kumamoto sequence. On 15 April 2016, an $M_w = 6.5$ earthquake occurred in the Kumamoto region, Japan[29], followed by a rich earthquake sequence considered to be aftershocks; 28 h later, an $M_w = 7.3$ earthquake revealed that these events were actually foreshocks. Both mainshocks caused severe damage. After the $M_w = 6.5$ earthquake, the Japan Meteorological Agency (JMA) warned of the possibility of large aftershocks with further damages. However, no information on an increased probability of $M_w = 7$ or larger earthquakes was made public because, according to the Earthquake Research Committee[30] protocol, the JMA had not considered the occurrence of larger earthquakes[31,32].

The Kumamoto sequence allows us to test our hypothesis in a different tectonic region and with mainshocks much closer together in time. We analyse the *b*-value time series for the source regions inferred for the $M_w = 6.5$ foreshock and for the $M_w = 7.3$ mainshock (Fig. 1a, b). For the background estimation, we select events in the JMA catalogue[29] starting in 2012 to avoid the first phase of the $M_w = 9$ Tohoku aftershocks. We divide the catalogue in three independent time periods: (1) from 2012 to the last event before the $M_w = 6.5$ earthquake (that is, the background), (2) from 1 h after the $M_w = 6.5$ earthquake to the last event before the mainshock and (3) from one day after the mainshock to the end of the catalogue (*b*-value time series) and the first two weeks of aftershocks (*b*-value map). The *b* values in the time interval between the two shocks are similar or below the background level ($b = 0.7$), a result confirmed in the frequency–magnitude distributions (Fig. 2c) and in the differential map (Fig. 2g). Once the $M_w = 7.3$ event occurs, however, the *b* values of the subsequent events increase strongly by 20–40%. Consequently, whereas the annualized probability of an $M_w = 7.3$ event in the 28 h in period (2) increased by a factor of 1,000, it decreased after the second mainshock to almost background levels (Fig. 1d). Again, no subsequent large event has occurred so far.

The 2011 Tohoku sequence

The 2011 $M_w = 9$ Tohoku event and its $M_w = 7.3$ foreshock, recorded just two days before the mainshock, represent a further case study from a very different tectonic regime. The *b* values before and after the $M_w = 9$ earthquake have already been mapped by Tormann et al.[33]. The limits of the seismic network in precisely localizing off-shore events and the resulting scatter in hypocentres do not allow us to apply our method to the $M_w = 7.3$ box without increasing the selection radius to 12 km in order to have a sufficiently large dataset. We estimate a background *b* value of 0.62 (Fig. 3a), the *b* value in between (0.44; a 73% decrease) and the aftershock *b* value on the $M_w = 7.3$ fault (0.9; a 150% increase over the background). Differential *b*-value mapping cannot be performed owing to the paucity of events above the magnitude of completeness, M_c, in the short interval between the $M_w = 7.3$ and $M_w = 9$ events.

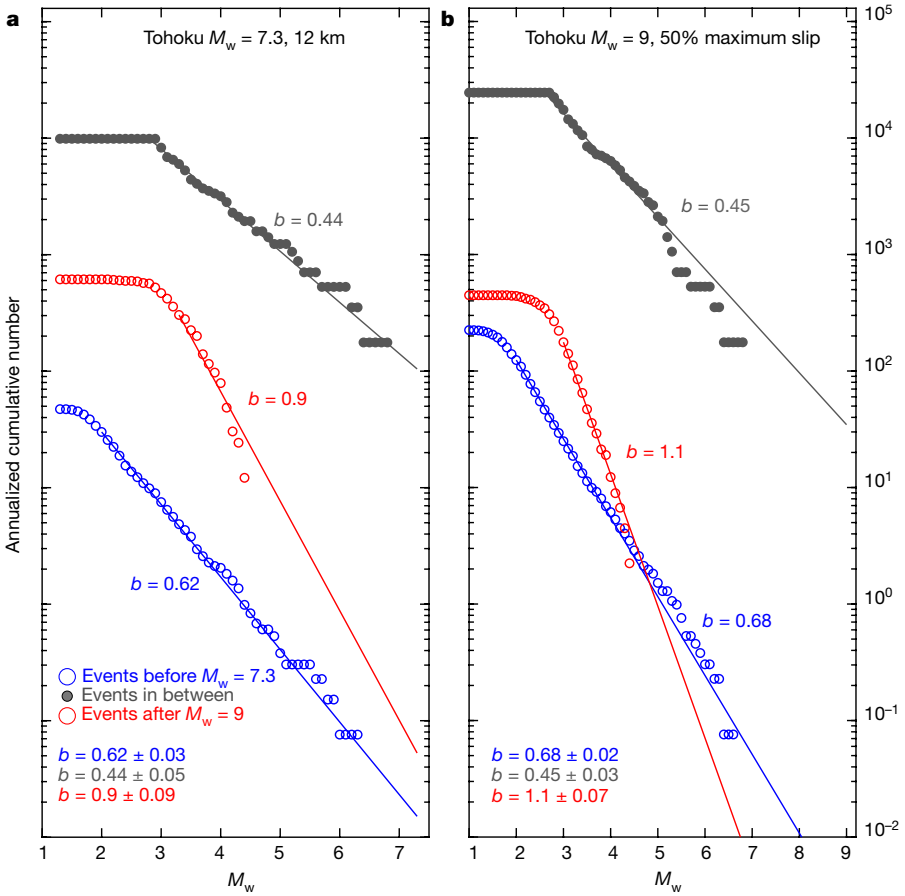

Fig. 3 | Frequency–magnitude distributions for the Tohoku case study. Frequency–magnitude distributions for three different periods of events within 12 km of the rupture plane of the $M_w = 7.3$ event (uncertainty from Shi and Bolt[47]). **b**, As in **a**, but for the events contained within 50% of the maximum slip contour of the $M_w = 9$ mainshock.

The *b* value within 50% of the maximum slip contour behaved similarly (from 0.68 to 0.45 to 1.1; Fig. 3b).

Possible physical mechanism

Currently, there are two schools of thought regarding foreshock mechanisms and prognostic value[34,35]: (i) the deterministic point of view, which supports that foreshocks represent a precursory process, for example, a response to precursory slip on the fault[16,33,36], and (ii) the stochastic point of view, which considers foreshocks to be an indistinguishable part of earthquake clustering[17], described through a statistical process such as the ETAS model[7,8]. According to the ETAS model, there is no difference between foreshocks, mainshocks and aftershocks; all foreshocks are mainshocks with aftershocks that happen to be bigger. The rupture process is not cyclic but epidemic.

We interpret the observed drop in *b* value documented in Figs. 1, 2 in a probabilistic framework of changes in the relevant stress conditions, which reconciles the aforementioned interpretations. Earthquakes of magnitude 6 and larger greatly perturb the stress field in the Earth crust. The amplitudes of the static- and dynamic-stress transfer decay with distance[37], and can both encourage and inhibit rupture. Under most conditions, this stress change will decrease the differential stress on nearby faults, thus increasing the *b* value[24]. However, under certain conditions, the differential stress on nearby and already tectonically loaded faults can increase instead, leading to a drop in *b* value and a subsequent much larger chance of an even stronger event. Conditions that favour such drops in *b* value are probably the presence of critically pre-stressed faults and overall high stress levels, as well as a suitable orientation of the source and receiver faults. It is also possible that continued post-seismic slip, the impact of secondary aftershocks or precursory processes, such as deep precursory slip, may play a role. Considering the numerous unknowns, we are currently unable to model individual sequences with sufficient reliability even a posteriori, and real-time modelling for warning purposes would be even more challenging. However, we can use the empirical observations of *b*-value changes as an input to improve earthquake risk mitigation.

Towards real-time risk mitigation

Our results (Figs. 1, 2) suggest that the evolution of *b* values, analysed as a proxy for the average stress conditions of faults in the regions, can act as a first-order discriminator between normal aftershocks and likely precursory sequences. In the large majority of aftershock sequences, the *b* value increases substantially after a mainshock of magnitude 6 or larger, typically by 20%[24]. This overall increase can be observed within hours of a mainshock, if indeed the seismic network is capable of reliable location and magnitude determination, and observing an increase in *b* lowers the probability of a subsequent larger event by maybe an order of magnitude (Figs. 1d, 2d). If, on the other hand, *b* remains the same or if it decreases considerably, then the probability of an even larger event is increased by several orders of magnitude.

We propose that our findings could be used to define a simple traffic light system expressing the level of concern associated with earthquakes. Traffic lights have been used to manage risk behaviour in a number of settings, such as food[38], health care[39], induced seismicity risk[40,41], volcanic eruption and in many other situations where decisions must be made in real time. They are a tool for recognizing risk in a quantitative way and then initiating risk reduction measures. The concept of our foreshock traffic light system (FTLS) is shown in Fig. 4. A yellow FTLS setting indicates that the *b* value remains mostly unchanged in the aftershock sequence or is difficult to determine. We define yellow, somewhat arbitrarily, as a ±10% change from the

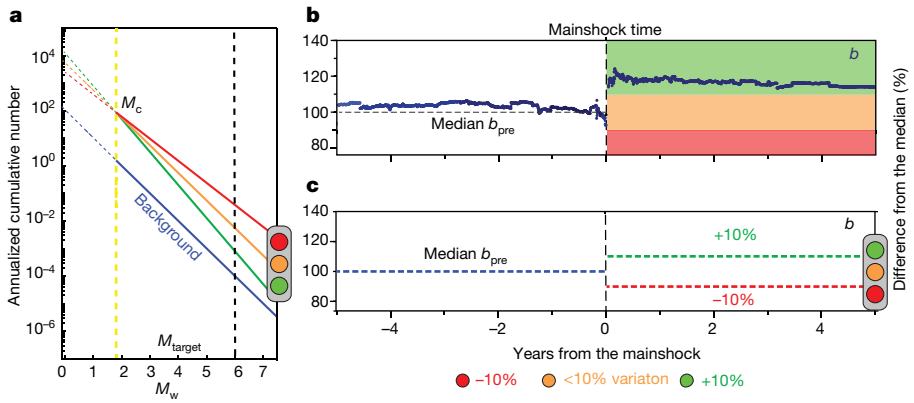

Fig. 4 | The foreshock traffic light system. a, **c**, Schematic representation of FTLS in the frequency–magnitude distribution view (**a**) and the *b*-value time series view (**c**). Green denotes an aftershock sequence with a *b*-value increase of about 20%, where no mainshock is expected; yellow indicates that the *b* value remains unchanged in the aftershock sequence or is difficult to determine; red means that the *b* value decreases considerably and mitigation actions must be considered. M_{target} is the reference value of *M* in the example. **b**, *b*-value stacking of 31 sequences, showing the per cent difference with respect to the reference value (that is, the median of the background *b* values, b_{pre}; black horizontal dashed line)[24]. The black vertical dashed line represents the time of the mainshock, shifted to zero.

background. Yellow represents the concern level according to present knowledge, with no additional discriminating information. A green FTLS setting corresponds to an aftershock sequence with an increase in *b* value of 10% or more, and we postulate that more than 80% of all sequences will fall into this category. The ability to declare a green status would represent an important contribution to earthquake resilience, because it would greatly reduce uncertainty and concern and would allow a quicker return to normality, for example, by initiating rebuilding efforts. Finally, a red FTLS setting would be declared if the *b* value decreased substantially, by 10% or more. In such situations, emergency managers should be especially concerned and consider actions such as continuing evacuations. In the future, it may be possible to refine the thresholds that we propose here on the basis of additional data, risk–cost–benefit analysis and by considering the uncertainty in *b* values. We also suggest that spatially mapping relative changes in *b* value may help us to define the most likely area of a subsequent large event. In the case of the Norcia event (Fig. 1), we note that the event did occur to the north of Amatrice, in the areas of the strongest decrease of *b*.

We tested our FTLS retrospectively on 58 sequences[24]. We calculated the percentage difference between the background and the *b* value of the aftershocks, selecting all events within 3 km from the rupture area. This allowed us to obtain a robust value for 25 sequences, in addition to the values obtained for the foreshocks of the Norcia and Kumamoto sequences, resulting in a total of 29 sequences. Of these, 18 were classified as a green alert, 8 as yellow and 3 as red (Fig. 5). Only two of these mainshocks were followed by subsequent larger ones (Amatrice–Norcia and Kumamoto), which is in line with the 5% probability of a secondary larger event[3,4]. We also added the values of the 2011 $M_w = 9$ Tohoku sequence (red alert after the $M_w = 7.3$ event, green after the $M_w = 9$ earthquake); however, we did not use them in the statistical analysis because, as discussed above, the method had been adjusted for larger hypocentre uncertainties.

For a first-order assessment of the performance of FTLS, we count in a binary classifier system the successful alerts (true positives), false alerts (false positives), missed events (false negatives) and correct negatives (true negatives). We consider yellow alerts as neutral. In this metric, we score two successful alerts, one false alert, no missed events and 18 correct negatives. Using confusion matrix analysis, we compute an accuracy of 0.95. If we assume that the chance of a subsequent larger event is 5%, then the random chance of correctly identifying two out of two mainshocks, with only one false alert and no missed events is below 1%.

The one false-positive red alert follows the $M_w = 6.2$ event in Morgan Hill (1984). Because it occurred 35 years ago, we speculate that the data quality may be inferior. The performance of the forecasting method can be further improved if we also analyse the spatial footprint of the *b*-value changes, as indicated in Figs. 1g, h, 2g, h. We perform FTLS classification also for the Norcia and Kumamoto ($M_w = 7.3$) source regions (which are known only a posteriori) of these mainshocks. Before the mainshock, *b* decreases most sharply, by 55% in Norcia and 68% in Kumamoto ($M_w = 7.3$), resulting in two red alerts.

Our results demonstrate that changes in *b* can act as a discriminant. Our hypothesis is also consistent with a physical framework in which stress influences the relative size distribution, and hence the probability,

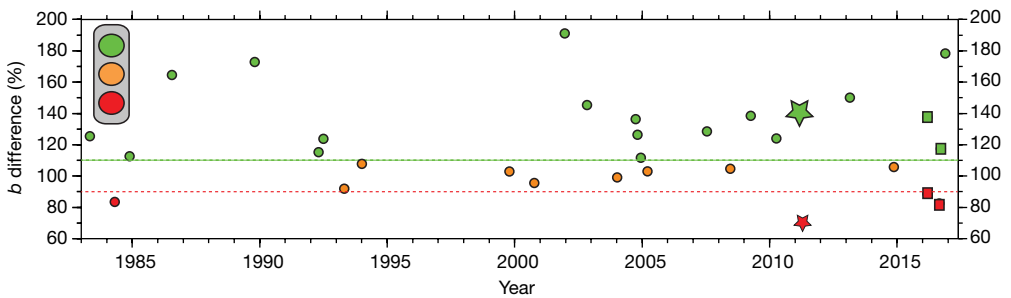

Fig. 5 | Performance analysis of the proposed foreshock traffic light system. Difference between the *b* values of aftershocks for 27 sequences recorded in California, Japan, Alaska and Italy (circles) and the background. Events are colour-coded by their FTLS class. The values obtained for the Amatrice and Kumamoto ($M_w = 6.5$) source regions (in between mainshocks and after the second mainshock) are shown as red squares; green squares indicate the values obtained for Norcia and Kumamoto ($M_w = 7.3$). The plotted events are listed in Table 1. The green star shows the extrapolated value for Tohoku, 2011, from figure 3 in Tormann et al.[33], and the red star represents the $M_w = 7.3$ Tohoku foreshock shown in Fig. 3.

Table 1 | *b*-value differences δb for the sequences in Fig. 5.

Name	Catalogue	Date	Mms	δb	FTLS colour
Coalinga	ANSS	2 May 1983	6.7	125%	Green
Morgan Hill	ANSS	24 Apr 1984	6.2	83%	Red
Round Valley	ANSS	23 Nov 1984	6.1	113%	Green
Chalfant Valley	ANSS	21 Jul 1986	6.4	164%	Green
Loma Prieta	ANSS	18 Oct 1989	7	173%	Green
Joshua Tree	ANSS	23 Apr 1992	6.1	115%	Green
Landers	ANSS	28 Jun 1992	7.3	124%	Green
Eureka Valley	ANSS	17 May 1993	6.1	92%	Yellow
Northridge	ANSS	17 Jan 1994	6.7	107%	Yellow
Hector Mine	ANSS	16 Oct 1999	7.1	103%	Yellow
San Simeon	ANSS	22 Dec 2003	6.5	99%	Yellow
Parkfield	ANSS	28 Sep 2004	6	136%	Green
El Mayor Cucapah	ANSS	4 Apr 2010	7.2	124%	Green
Tottori	JMA	6 Oct 2000	7.3	96%	Yellow
Ryukyu	JMA	18 Dec 2001	7.3	191%	Green
Chūetsu	JMA	23 Oct 2004	6.8	126%	Green
Southern Romoi	JMA	14 Dec2004	6.1	112%	Green
Fukuoka	JMA	20 Mar 2005	7	103%	Yellow
Chūetsu Offshore	JMA	16 Jul 2007	6.8	128%	Green
Iwate	JMA	13 Jun 2008	7.2	104%	Yellow
Awaji Island	JMA	12 Apr 2013	6.3	150%	Green
Nagano (for)	JMA	22 Nov 2014	6.7	105%	Yellow
Kumamoto (for)	JMA	14 Apr 2016	6.5	88%	Red
Kumamoto	JMA	15 Apr 2016	7.3	138%	Green
Fukushima	JMA	21 Nov 2016	7.4	178%	Green
L'Aquila	Gasperini et al.[27]	6 Apr 2009	6.3	139%	Green
Amatrice	Gasperini et al.[27]	24 Aug2016	6.2	83%	Red
Norcia	Gasperini et al.[27]	30 Oct 2016	6.5	116%	Green
Denali	AEIC	3 Nov 2002	7.6	145%	Green
Tohoku (for)	JMA	9 March 2011	7.3	73%	Red
Tohoku	JMA	11 March 2011	9	140%	Green

The last row shows the Tohoku increase according to Tormann et al.[33]. AEIC, Alaska Earthquake Information Center (http://earthquake.alaska.edu); ANSS, Advanced National Seismic System (https://earthquake.usgs.gov/monitoring/anss/); for, foreshock.

of a subsequent large event. However, there are several limitations to FTLS. First, the number of cases that we are able to investigate is still limited, because magnitude-6 or greater earthquakes are rare in areas with excellent network coverage. Especially lacking are more cases of true positives. An important implication of our work is, therefore, that seismic networks around the globe must substantially upgrade and further automate their processing procedures and increase in station density. Being able to detect and process magnitude-2 and larger events consistently and almost in real time during a vigorous 'aftershock' sequence is a major challenge that very few networks master today. The imprint of a mainshock on the size distribution of aftershocks decays away within a few kilometres of the rupture plane[24], so it is critically important to achieve relative hypocentre accuracies of around 1–2 km. This requirement currently limits, for example, the analysis of the $M_w = 7.3$ foreshock preceding the Tohoku $M_w = 9$ mainshock, or the compilation of an analysis-based global earthquake catalogue for systematic testing. However, promising improvements in seismic networks are on the way because, for example, template matching of all waveforms recorded against a large set of template events[42,43] is becoming computationally feasible. The Kumamoto case is especially important because it highlights that the FTLS approach can be applied within a few hours of the mainshock.

A further limitation is that we lack a better physics-based understanding and predictive modelling capability of precursory sequences. However, our hypothesis presents a new angle in which aftershock sequences can be understood and modelled. In addition, stimulated by our findings presented here, new laboratory-based, numerical and field-data-based studies will advance our understanding in the near future. There is also a clear need to test our hypothesis in a fully prospective sense—the gold standard of earthquake forecasting[44,45]. Such tests have been initiated and will take many years to complete with meaningful statistical power. We would advocate, however, that in regions of the world with sufficient network coverage, seismologists and energy managers should consider adopting our FTLS as additional information for decision-making during seismic crises.

Online content

Any methods, additional references, Nature Research reporting summaries, source data, extended data, supplementary information, acknowledgements, peer review information; details of author contributions and competing interests; and statements of data and code availability are available at https://doi.org/10.1038/s41586-019-1606-4.

Received: 10 February 2019; Accepted: 20 August 2019;
Published online 9 October 2019.

1. Jordan, T. H. et al. Operational earthquake forecasting state of knowledge and guidelines for utilization. *Ann. Geophys.* **54**, 315–391 (2011).
2. Lippiello, E., Giacco, F., Marzocchi, W., Godano, C. & de Arcangelis, L. Statistical features of foreshocks in instrumental and ETAS catalogs. *Pure Appl. Geophys.* **174**, 1679–1697 (2017).
3. Reasenberg, P. A. & Jones, L. M. California aftershock hazard forecast. *Science* **247**, 345–346 (1990).
4. Roeloffs, E. & Goltz, J. The California earthquake advisory plan: a history. *Seismol. Res. Lett.* **88**, 784–797 (2017).
5. Field, E. H. et al. The potential uses of operational earthquake forecasting. *Seismol. Res. Lett.* **87**, 313–322 (2016).
6. Zechar, J. D., Marzocchi, W. & Wiemer, S. Operational earthquake forecasting in Europe: progress, despite challenges. *Bull. Earthquake Eng.* **14**, 2459–2469 (2016).
7. Ogata, Y. Statistical models for earthquake occurrences and residual analysis for point processes. *J. Am. Stat. Assoc.* **83**, 9–27 (1988).
8. Ogata, Y. Space-time point-process models for earthquake occurrences. *Ann. Inst. Stat. Math.* **50**, 379–402 (1998).
9. Gerstenberger, M. C., Wiemer, S., Jones, L. M. & Reasenberg, P. A. Real-time forecasts of tomorrow's earthquakes in California. *Nature* **435**, 328–331 (2005).
10. Parsons, T. et al. Stress-based aftershock forecasts made within 24 h postmain shock: expected north San Francisco Bay area seismicity changes after the 2014 $M = 6.0$ West Napa earthquake. *Geophys. Res. Lett.* **41**, 8792–8799 (2014).
11. Stein, R. Earthquake conversations. *Sci. Am.* **288**, 72–79 (2003).
12. Woessner, J. et al. A retrospective comparative forecast test on the 1992 Landers sequence. *J. Geophys. Res.* **116**, B05305 (2011).
13. van Stiphout, T., Wiemer, S. & Marzocchi, W. Are short-term evacuations warranted? Case of the 2009 L'Aquila earthquake. *Geophys. Res. Lett.* **37**, L06306 (2010).
14. Gulia, L., Tormann, T., Wiemer, S., Herrmann, M. & Seif, S. Short-term probabilistic earthquake risk assessment considering time-dependent *b* values. *Geophys. Res. Lett.* **43**, 1100–1108 (2016).
15. Brodsky, E. E. & Lay T. Recognizing foreshocks from the 1 April 2014 Chile earthquake. *Science* **344**, 700–702 (2014).
16. Bouchon, M., Durand, V., Marsan, D., Karabulut, H. & Schmittbuhl, J. The long precursory phase of most large interplate earthquakes. *Nat. Geosci.* **6**, 299–302 (2013).
17. Ellsworth, W. L. & Bulut, F. Nucleation of the 1999 Izmit earthquake by a triggered cascade of foreshocks. *Nat. Geosci.* **11**, 531–535 (2018).
18. Gutenberg, B. & Richter, C. F. Frequency of earthquakes in California. *Bull. Seismol. Soc. Am.* **34**, 185–188 (1944).
19. Ishimoto, M. & Iida, I. Observations of earthquakes registered with the microseismograph constructed recently. *Bull. Earthquake Res. Inst. Univ. Tokyo* **17**, 443–478 (1936).
20. Goebel, T. H. W., Schorlemmer, D., Becker, T. W., Dresen, G. & Sammis, C. G. Acoustic emissions document stress changes over many seismic cycles in stick-slip experiments. *Geophys. Res. Lett.* **40**, 2049–2054 (2013).
21. Amitrano, D. Brittle-ductile transition and associated seismicity: Experimental and numerical studies and relationship with the *b* value. *J. Geophys. Res.* **108**, 1–15 (2003).

22. Scholz, C. H. The frequency-magnitude relation of microfracturing in rock and its relation to earthquakes. *Bull. Seismol. Soc. Am.* **58**, 399–415 (1968).
23. Schorlemmer, D., Wiemer, S. & Wyss, M. Variations in earthquake-size distribution across different stress regimes. *Nature* **437**, 539–542 (2005).
24. Gulia, L. et al. The effect of a mainshock on the size distribution of the aftershocks. *Geophys. Res. Lett.* **45**, 13277–13287 (2005).
25. Helmstetter, A. Comparison of short-term and time-independent earthquake forecast models for southern California. *Bull. Seismol. Soc. Am.* **96**, 90–106 (2006).
26. Vannucci, G., Gasperini, P., Lolli, B. & Gulia, L. Fast characterization of sources of recent Italian earthquakes from macroseismic intensities. *Tectonophysics* **750**, 70–92 (2019).
27. Gasperini, P., Lolli, B. & Vannucci, G. Empirical calibration of local magnitude data sets versus moment magnitude in Italy. *Bull. Seismol. Soc. Am.* **103**, 2227–2246 (2013).
28. Wiemer, S. & Wyss, M. Mapping the frequency-magnitude distribution in asperities: an improved technique to calculate recurrence times? *J. Geophys. Res.* **102**, 15115–15128 (1997).
29. Japan Meteorological Agency. *JMA catalogue* http://www.data.jma.go.jp/svd/eqev/data/bulletin/index_e.html.
30. Earthquake Research Committee. *Evaluation of the 2016 Kumamoto Earthquakes* (ERC, 2016); https://www.jishin.go.jp/main/chousa/16may_kumamoto2/index-e.htm.
31. Nanjo, K.Z. & Yoshida, A. Anomalous decrease in relatively large shocks and increase in the p and b values preceding the April 16, 2016, M 7.3 earthquake in Kumamoto, Japan. *EPS* **69**, 13 (2017).
32. Omi, T. et al. Implementation of a real-time system for automatic aftershock forecasting in Japan. *Seismol. Res. Lett.* **90**, 242–250 (2019).
33. Tormann, T., Enescu, B., Woessner, J. & Wiemer, S. Randomness of megathrust earthquakes implied by rapid stress recovery after the Japan earthquake. *Nat. Geosci.* **8**, 152–158 (2015).
34. Gomber, J. Unsettled earthquake nucleation. *Nat. Geosci.* **11**, 463–464 (2018).
35. Mignan, A. The debate on the prognostic value of earthquake foreshocks: a meta-analysis. *Sci. Rep.* **4**, 4099 (2014).
36. Tape, C. et al. Earthquake nucleation and fault slip complexity in the lower crust of central Alaska. *Nat. Geosci.* **11**, 536–541 (2018); author correction 11, 615 (2018).
37. Okada, Y. Internal deformation due to shear and tensile faults in a half-space. *Bull. Seismol. Soc. Am.* **82**, 1018–1040 (1992).
38. European Commission. *A Strategy for Europe on Nutrition, Overweight and Obesity Related Health Issues. White Paper COM (2007)* **279** (European Commission, 2007); https://ec.europa.eu/health/ph_determinants/life_style/nutrition/documents/nutrition_wp_en.pdf.
39. Department of Health. *Information for a Healthy New York: Asthma Action Plan* (New York State Department of Health, 2002); www.health.state.ny.us/diseases/asthma/pdf/4850.pdf.
40. Bommer, J. J. et al. Control of hazard due to seismicity induced by a hot fractured rock geothermal project. *Eng. Geol.* **83**, 287–306 (2006).
41. Mignan, A., Broccardo, M., Wiemer, S. & Giardini, D. Induced seismicity closed-form traffic light system for actuarial decision-making during deep fluid injections. *Sci. Rep.* **7**, 13607 (2017).
42. Li, Z. F., Meier, M. A., Hauksson, E., Zhan, Z. W. & Andrews, J. Machine learning seismic wave discrimination: application to earthquake early warning. *Geophys. Res. Lett.* **45**, 4773–4779 (2018).
43. Shelly, D. R. A 15 year catalog of more than 1 million low-frequency earthquakes: tracking tremor and slip along the deep San Andreas Fault. *J. Geophys. Res. Solid Earth* **122**, 3739–3753 (2017).
44. Jordan, T. H. Earthquake predictability, brick by brick. *Seismol. Res. Lett.* **77**, 3–6 (2006).
45. Schorlemmer, D. et al. The collaboratory for the study of earthquake predictability: achievements and priorities. *Seismol. Res. Lett.* **89**, 1305–1313 (2018).
46. Wells, D. L. & Coppersmith, K. J. New empirical relationships among magnitude, rupture length, rupture width, rupture area, and surface displacement. *Bull. Seismol. Soc. Am.* **84**, 974–1002 (1994).
47. Shi, Y. & Bolt, B. A. The standard error of the magnitude-frequency *b* value. *Bull. Seismol. Soc. Am.* **72**, 1677–1687 (1982).
48. Dziewonski, A. M., Chou, T. A. & Woodhouse, J. H. Determination of earthquake source parameters from waveform data for studies of global and regional seismicity. *J. Geophys. Res.* **86**, 2825–2852 (1981).
49. Ekström, G., Nettles, M. & Dziewoński, A. M. The global CMT project 2004–2010: centroid-moment tensors for 13,017 earthquakes. *Phys. Earth Planet. Inter.* **200–201**, 1–9 (2012).
50. Wiemer, S. & Wyss, M. Minimum magnitude of completeness in earthquake catalogs: examples from Alaska, the Western United States, and Japan. *Bull. Seismol. Soc. Am.* **90**, 859–869 (2000).
51. Woessner, J. & Wiemer, S. Assessing the quality of earthquake catalogues: estimating the magnitude of completeness and its uncertainty. *Bull. Seismol. Soc. Am.* **95**, 684–698 (2005).
52. Tormann, T., Wiemer, S. & Mignan, A. Systematic survey of high-resolution b value imaging along Californian faults: inference on asperities. *J. Geophys. Res.* **119**, 2029–2054 (2014).

METHODS

The method that we propose for real-time discrimination between foreshock and aftershock sequences and that we apply to the Kumamoto and Amatrice–Norcia sequences is composed of the following steps.

Selecting events near the rupture plane of the initiating event. (1) The focal mechanism[48,49], which is available within minutes to hours after the origin time of a moderate-to-large initiating earthquake (here we consider a magnitude of 6 or larger), provides the information required to build a first-order source model: the magnitude, strike, dip and rake of the two possible nodal planes. Here we use the focal mechanism provided by the global centroid moment tensor solution because it is harmonized and available for all events studied (but other solutions are equally possible). Using the empirical formulas of Wells and Coppersmith[46], we model the two nodal planes: the length and width are derived directly from the magnitude and the rake, the three-dimensional orientation is given by strike and dip (see ref. [46] and our code presented here for the relevant equations for normal, strike-slip and reverse regimes or the general case).

(2) We then adjust the hypocentre of the initiating event to the one reported by the local network, because global centroid moment tensor hypocentres are much less accurate and we need to ensure consistency between after- and foreshocks and the initiating event.

(3) To determine the actual fault plane automatically, we select all events recorded in the sequences within three kilometres of each of the nodal planes and then choose the plane where most of the supposed aftershocks are located in. This we assume to be the source volume, referred to from here on as 'the box'. Typically, one to several hours of aftershocks are sufficient to select the right plane, and rapid source-inversion approaches can also deliver a finite fault model within 1–2 h.

Constructing the time series. (4) We divide the dataset into two parts: a pre- and a post-initiating-event catalogue. The start time of the pre-event catalogue depends on the quality and completeness of the local network and sometimes on avoiding overlap with past sequences (in our case, we choose 1 January 2012 for both Japan and Italy; in Italy, to avoid overlap with the L'Aquila aftershocks and in Kumamoto to avoid the influence of the 2011 Tohoku $M_w = 9$ megathrust event). The pre-event period should ideally contain several years of seismicity for a robust estimate. The post-event catalogue is then updated as new events emerge; in our case we analyse the subsequent two years of aftershocks.

(5) The two sub-catalogues are cut at magnitude 1, and then we compute the overall M_c using the maximum-curvature method[50]. This defines the overall minimum M_c level needed to make the sample-specific M_c assessment more robust.

(6) Next, we estimate a pre-event reference b value. We distinguish two cases, depending on the abundance of the events within the box:

(a) If more than a user-defined minimum number of events (N_{pre}) are available, we compute a time series. This is done by first re-assessing completeness for the first sample of 250 events using the maximum-curvature method but adding a correction factor of +0.2 (as recommended by Woessner and Wiemer[51]). As additional quality assurance steps, we require at least 50 events above completeness and also check if the sample passes the linearity test described in Tormann et al.[52]. The b and a values and their respective uncertainties are computed using a maximum-likelihood assessment[47]. The window is then moved forward by one event and the background reference b value is computed as the median of all individual b values in this time series.

(b) If fewer than N_{pre} events are available, we use the N_{pre} events that are nearest to the epicentre and then compute a single regional background b value as reference, following the computational approach defined in (a). This procedure was used for the $M_w = 6.5$ Kumamoto event (Fig. 2a), sampling a distance of up to 17 km from the epicentre.

(7) We estimate the post-event time series of b values. We first remove the events recorded in the initial part of the sequence, which is typically highly incomplete and heterogeneous. This exclusion period depends on the quality of the seismic network and is an expert's choice. We then compute a time series of b values again by the approach described in (a); however, we use a sample size of $N_{post} = 400$ to increase robustness and because aftershock sequences are very data-rich. We plot the time series and its uncertainty in Figs. 1, 2 and compute the per cent change with respect to the reference b value. If the difference exceeds +10% or −10%, we assign a traffic light colour of green or red, respectively; otherwise we assign orange (Fig. 3).

(8) The procedure described in (7) is repeated after the second mainshocks.

The main free parameters in our analysis are N_{pre} and N_{post}. We tested that the results of our analysis do not critically depend on the choice of these parameters within reasonable ranges (for example, $N_{pre} = 150$–300, $N_{post} = 250$–500).

Mapping *b*-value changes. As additional information, we assess the spatial footprint of b-value changes (Figs. 1, 2g, h). The b-value maps are computed using ZMAP 7.0 (available at http://www.seismo.ethz.ch/en/research-and-teaching/products-software/software/ZMAP/) and post-processed using Matlab and Generic Mapping Tool. The relevant input parameters are:

(I) Background b-value map. On a regularly spaced grid of 2 km, the closest 250 events above the pre-cut M_c of 1.0 are sampled, up to a maximum radius of 15 km. The node-specific M_c is then estimated by the maximum-curvature method[51], by adding a 0.2 correction[50]. The b values are computed using the maximum-likelihood method[47] (Figs. 1, 2f).

(II) Post-initiating-event maps. The same procedure is applied, but we use 400 events and add a correction of 0.4 to account for the more heterogeneous data. For these two intervals, we plot the per cent difference in b value with respect to the background (Figs. 1, 2g, h).

Data and code availability

The datasets generated and analysed during the current study, as well as the Matlab codes written for the analysis, are available at https://doi.org/10.3929/ethz-b-000357449.

Acknowledgements The figures were produced with the Generic Mapping Tool (http://gmt.soest.hawaii.edu). b-value maps were created with ZMAP (http://www.seismo.ethz.ch/en/research-and-teaching/products-software/software/ZMAP/).

Author contributions L.G. and S.W. conceived the analysis method and wrote the paper. L.G. performed the data analysis and created the figures.

Competing interests The authors declare no competing interests.

Additional information

Supplementary information is available for this paper at https://doi.org/10.1038/s41586-019-1606-4.

Correspondence and requests for materials should be addressed to L.G.